Chinese Chemical Letters 37 (2026) 112153

Contents lists available at ScienceDirect

Chinese Chemical Letters

journal homepage: www.elsevier.com/locate/cclet

Plasma-engineered activated carbon fibers for boosting sulfate selectivity and regeneration performance in room-temperature malodorous H_2S catalytic oxidation

Yue Liu[a], Linhong Wen[a], Mengyan Wang[b], Jianxiao Yang[a,*], Xin Zhang[b,*]

[a] *Hunan Province Key Laboratory for Advanced Carbon Materials and Applied Technology, College of Materials Science and Engineering, Hunan University, Changsha 410082, China*

[b] *College of Resources and Environment, University of Chinese Academy of Sciences, Beijing 101408, China*

ARTICLE INFO

Article history:
Received 13 June 2025
Revised 22 October 2025
Accepted 21 November 2025
Available online 21 November 2025

Keywords:
Activated carbon fibers
H_2S catalytic oxidation
Plasma defect engineering
Sulfate selectivity
Water regeneration

ABSTRACT

Catalytic oxidation of H_2S at room temperature has been regarded as a promising method for removing malodorous H_2S pollution. However, most of the existing research has primarily focused on developing catalysts with high sulfur capacity, *i.e.*, high elemental sulfur selectivity, which was unfavored for the catalyst regeneration. The present work prioritizes efficient water wash regeneration as a key objective. A series of activated carbon fibers (ACFs) was synthesized using a synergistic strategy of "nitrogen doping-plasma defect engineering". The certain amount of nitrogen species ensured a certain level of sulfur capacity. The plasma defect engineering can result in the enhancement of surface acidity and defect density, which worked together to make the catalyst with high sulfate selectivity. The O_2-plasma modified NH_3-ACF-O10 catalyst achieved the best catalytic performance with appropriate sulfur capacity (0.21 g/g) and highest sulfate selectivity (85.40 %). Importantly, it can be easily regenerated by water wash, and almost 83.33 % sulfur capacity can be recovered. Besides, superoxide radicals ($O_2^{\bullet-}$) were identified as the primary reactive oxygen species for the reaction. And the reaction obeyed a Langmuir-Hinshelwood (L-H) like mechanism, *i.e.*, the reaction was proceeded *via* chemisorbed H_2S and $O_2^{\bullet-}$, which was adsorbed and activated by defect.

© 2026 Published by Elsevier B.V. on behalf of Chinese Chemical Society and Institute of Materia Medica, Chinese Academy of Medical Sciences.

In recent years, the issue of odor control has become increasingly significant due to the rising civil complaints and growing concerns regarding environmental and public health [1–3]. The primary gas responsible for malodor is hydrogen sulfide (H_2S), which is emitted at high concentrations (around 100 ppm) and presents a considerable challenge in pollution management due to its extremely low olfactory threshold [4,5]. Currently, a variety of methods have been developed to remove H_2S, including *in situ* precipitation, absorption, and room-temperature catalytic oxidation, among others [6,7].

Among various catalytic methods, H_2S catalytic oxidation at room temperature is regarded as the most promising due to its simplicity and cost-effectiveness [4]. During the reaction, H_2S reacts catalytically with oxygen under moist conditions to produce elemental sulfur and sulfate. As the reaction progresses, the products accumulate in the catalyst's pores and on its surface until its storage capacity becomes fully saturated [8,9]. Therefore, identifying suitable catalysts has become the central focus for optimizing this process. Significant progress has been made in the field of metal oxide catalysts, and a deeper understanding of the underlying reaction mechanisms has led to the development of advanced catalytic materials [10–12]. However, due to their inherent susceptibility to deactivation under humid and sulfur-rich conditions, metal oxides are not well-suited for this process. In contrast, carbon-based catalysts are emerging as promising candidates for room-temperature H_2S oxidation, owing to their tunable surface chemistry and high specific surface area [13–15]. Nevertheless, the catalytic efficiency of pure carbon materials is limited by the absence of both basic and active sites. To enhance the catalytic performance of carbon-based materials, various strategies have been adopted, including heteroatom doping and metal single-atom modification, which enable efficient and selective oxidation of H_2S [16–19]. Among these strategies, nitrogen doping has become one of the most prominent methods for enhancing the sulfur capacity of carbon materials [20–22]. Nitrogen atoms, due to their difference in electronegativity, act as Lewis basic sites, facilitating the adsorp-

* Corresponding authors.
E-mail addresses: yangjianxiao@hnu.edu.cn (J. Yang), xzhang@ucas.ac.cn (X. Zhang).

https://doi.org/10.1016/j.cclet.2025.112153
1001-8417/© 2026 Published by Elsevier B.V. on behalf of Chinese Chemical Society and Institute of Materia Medica, Chinese Academy of Medical Sciences.

tion and dissociation of H_2S [23,24]. However, the practical application of nitrogen-doped carbon materials is significantly hindered by regeneration challenges. A higher sulfur capacity often leads to elemental sulfur as the primary reaction product, which is difficult to remove from the catalyst surface, thus limiting the catalyst's long-term performance.

It is worth noting that the catalyst can be regenerated readily using a water-wash method if the predominant product of the reaction can be shifted to water-soluble sulfate, that is, the catalyst with high sulfate selectivity. Extensive research has demonstrated that both porosity and surface acidity are important for the sulfate selectivity [25–27]. It is believed that acidic surfaces and small micropores (pore size less than 0.7 nm) are conducive to sulfate formation [8,28,29]. However, it is reported that the sulfate selectivity can only reach 52.58 % through the modification of the catalyst's porosity and surface acidity [30]. Significantly, superoxide radicals ($O_2^{\bullet-}$) have been detected during the reaction over modified carbon materials in recent studies, which can lead to the direct oxidation of H_2S to sulfate by considering the highly reactive of these radicals. At the current stage of knowledge, ultra-micropores, carbon defect sites and doped heteroatoms (N, S, B, P) can be regarded as active sites that activate O_2 to form $O_2^{\bullet-}$ [31–34].

Therefore, more radical active sites lead to the generation of more radicals, and consequently, high sulfated selectivity can be achieved. Enhancing the defect density on the surface of carbon materials has emerged as a key strategy to boost radical generation and improve sulfate selectivity, especially in light of the limited heteroatom content in the carbon framework and the higher mass transfer resistance associated with ultra-micropores during the reaction. However, it should be noted that the achievement of both high sulfate selectivity and high sulfur capacity is inherently contradictory in principle. Namely, high sulfate selectivity always means relative low sulfur capacity.

Therefore, developing catalyst with both high sulfate selectivity and appropriate sulfur capacity is a major challenge.

In the present work, a "nitrogen doping-defect engineering" synergy strategy was employed out on activated carbon fibers (ACFs) materials. First, ACFs were treated and activated under an ammonia atmosphere. Plasma defect engineering was then further applied to modify the nitrogen-doped ACFs. Hence, the doped nitrogen species can serve as basic sites and enhance the sulfur capacity. Meanwhile, the plasma treatment, in combination with NH_3 etching, can introduce defects on the surface of ACFs and facilitate the activation of oxygen to radicals. Additionally, the doped nitrogen atoms can contribute to the formation of defects as well and can be considered as extrinsic defects. Subsequently, the catalytic performance, regeneration performance, and the reaction mechanism were thoroughly evaluated and investigated.

Fig. 1a showed the preparation process of plasma engineered N doped ACFs. The SEM images of the modified ACFs were depicted in Figs. 1b-e. It is shown that ACFs exhibited a rough surface after plasma-modified due to the plasma etching, where the active species (N_2, air and O_2) colliding with the surface. Additionally, it was evident that the extent of surface roughness strongly depended on the reactivity of the active species (N_2 < air < O_2) and followed the order: NH_3-ACF-N10 < NH_3-ACF-A10 < NH_3-ACF-O10. Among these, NH_3-ACF-O10 exhibited the highest surface roughness.

The N_2 adsorption-desorption isotherms of the synthesized ACFs were presented in Fig. 1f. All isotherms exhibited the characteristics of typical type I, indicating that all the samples were dominated by micropore structures [35–37]. Table 1 summarized the specific surface area, pore volume, and pore size of the prepared ACFs. It was noteworthy that both the S_{BET} and pore volume decreased markedly after plasma treatment. Specifically, the values were 1366, 1332, 1212, and 1064 m^2/g for NH_3-ACF, NH_3-ACF-N10, NH_3-ACF-A10 and NH_3-ACF-O10, respectively. Moreover, the decreasing trend was in perfect agreement with the increase in surface roughness. In other words, the greater the reactivity of the active species, the more pores collapsed, leading to a reduction in both the S_{BET} and V_{tot}. However, plasma modification had minimal impact on pore size and distribution, as illustrated in Fig. 1g, where all samples displayed comparable pore dimensions.

XPS analysis was additionally performed to examine the chemical composition and characteristics of the prepared ACFs. The spectra (Fig. S1 in Supporting information) revealed that C, N, O elements are presented on the surface for all the samples, indicating the successfully introduction of nitrogen species. Regarding surface nitrogen content, as shown in Fig. 1h, it was 1.28, 2.43, 1.79, and 1.04 at% for NH_3-ACF, NH_3-ACF-N10, NH_3-ACF-A10 and NH_3-ACF-O10, respectively. In other words, the nitrogen content increased after N_2 and air plasma modification, however, decreased after O_2 plasma. Meanwhile, the surface oxygen content increased significantly for all the plasma modified samples. As demonstrated in Fig. 1i, the content of surface oxygen content in the NH_3-ACF, NH_3-ACF-N10, NH_3-ACF-A10 and NH_3-ACF-O10 ranges were 6.13, 12.78, 13.93, and 11.89 at%, respectively. As is known that the plasma modification process is comprised of two distinct stages. The initial stage encompasses the introduction of nitrogen and oxygen containing functional groups. However, for the second stage, the carbon atom, the introduced nitrogen and oxygen atoms will be further removed partially as processing time progresses and plasma power increased [38]. Therefore, both the nitrogen and oxygen content of NH_3-ACF-A10 and NH_3-ACF-O10 catalysts decreased significantly compared with NH_3-ACF-N10, which can be explained by the fact that the active substances air and oxygen can cause more oxygen and nitrogen species remove in the second stage. It was noteworthy that the removal of carbon and nitrogen atoms from the carbon framework may lead to the creation of vacancies due to the rearrangement of the sp^2 hybridized carbon network [34,39,40]. This observation reinforced the notion that plasma modification effectively promoted the formation of defects on the catalyst surface. More important, the N content of the prepared catalyst was extremely low comparing to the literature reports, which was in the range of 5.00–20.00 at% [21,22,24].

Moreover, as depicted in Fig. S2 (Supporting information), the oxygen species were further classified into C=O species (531.1 eV), C–OH/C–O-C species (532.2 eV), COOCO species (533.3 eV) and COOH species (534.2 eV) [41]. In a similar manner, the N 1s spectra (Fig. 1j and Fig. S3 in Supporting information) were deconvoluted into four peaks corresponding to binding energies of 398.5, 400.0, 401.0 and 403.0 eV, attributable to pyridinic-N atoms (PdN), pyrroline-N atoms (PyN), quaternary-N atoms (GrN), and pyridine-*N*-oxide (N-X), respectively [42]. Notably, PdN content decreased significantly after plasma modification due to the transformation of nitrogen species to the more stable GrN and N-X species under the high energy of the plasma process. The PdN content was 0.81, 0.57, 0.42, and 0.27 at% for NH_3-ACF, NH_3-ACF-N10, NH_3-ACF-A10 and NH_3-ACF-O10, respectively. PdN was considered the most important nitrogen species for the reaction because it provided basic anchoring sites to capture acidic H_2S. As illustrated in Fig. 1k, the water contact angles of the plasma-modified ACFs did not exhibit significant differences. Specifically, the water contact angles of NH_3-ACF, NH_3-ACF-N10, NH_3-ACF-A10, and NH_3-ACF-O10 were measured at 95°, 88°, 88°, and 87°, respectively. However, the hydrophilic properties were slightly enhanced after plasma modification, which could be attributed to the relatively increased content of oxygen-containing functional groups.

As illustrated in Fig. 2a, Raman spectroscopy was used to analyze the intensity ratio of the D-band to the G-band (I_D/I_G) in the ACFs, which was sensitive to defects [24]. The findings shown an increase in the I_D/I_G ratio for all plasma-modified samples (Fig.

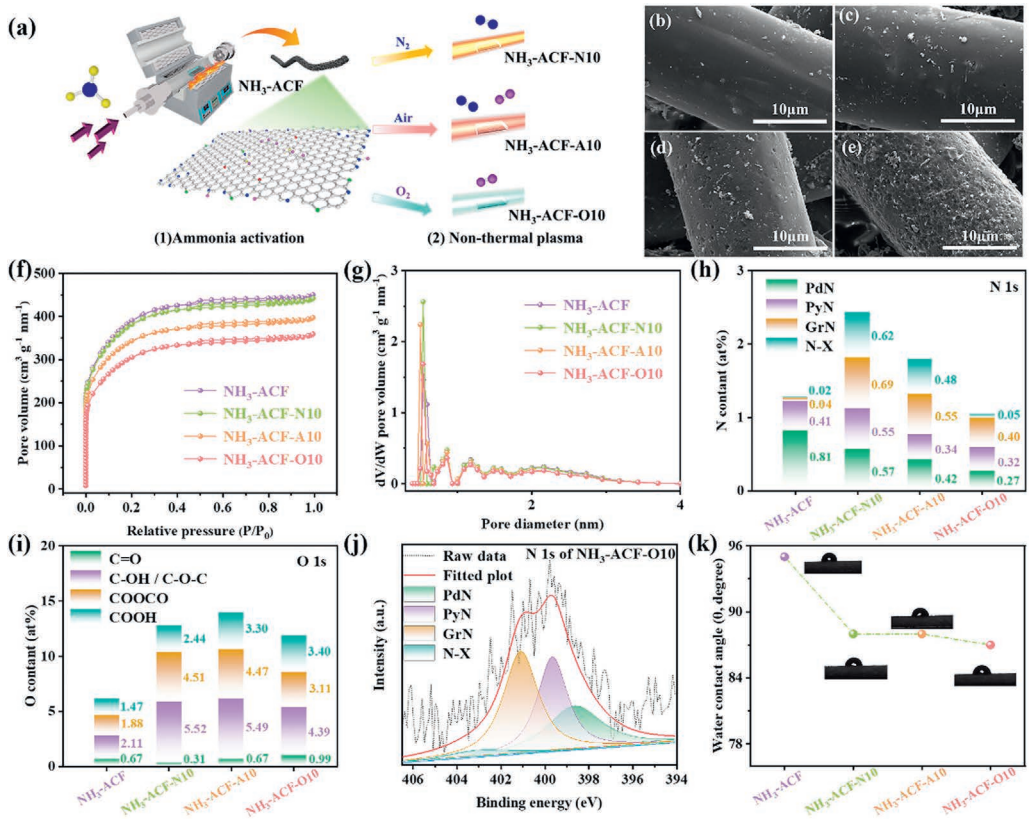


Fig. 1. (a) The preparation of NH_3-ACFs and NH_3-ACF-X, SEM images of NH_3-ACF (b), NH_3-ACF-N10 (c), NH_3-ACF-A10 (d), and NH_3-ACF-O10 (e). N_2 adsorption-desorption isotherms (f), pore size distribution (g), the composition of nitrogen species (h), the composition of oxygen species (i), the high-resolution N 1s XPS spectra of NH_3-ACF-O10 (j) and water contact angle of ACFs (k).

Table 1
Pore structure parameters of ACFs.

Samples	S_{BET} (m^2/g)	V_{mic} (cm^3/g)	V_{mes} (cm^3/g)	V_{tot} (cm^3/g)	V_{mic}/V_{tot} (%)	D_{ave} (nm)
NH_3-ACF	1366	0.51	0.19	0.70	72.86	2.04
NH_3-ACF-N10	1332	0.49	0.19	0.68	72.06	2.05
NH_3-ACF-A10	1212	0.45	0.16	0.61	73.77	2.03
NH_3-ACF-O10	1064	0.40	0.16	0.56	71.43	2.09

2b), with values of 1.19, 1.25, 1.30 and 1.35 for NH_3-ACF, NH_3-ACF-N10, NH_3-ACF-A10 and NH_3-ACF-O10, respectively. To further analysis defect density (n_D, cm^{-2}), the following Cançado's equation Eq. 1 was used to quantify [43].

$$n_D\left(cm^{-2}\right) = (7.32 \pm 2.2) \times 10^9 {E_L}^4 (I_D/I_G) \quad (1)$$

where E_L is specified as excitation energy, which is set to 2.41 eV in this work.

As demonstrated in Table S1 (Supporting information), upon subjecting the samples to plasma treatment, the observed change in n_D values exhibited consistency with I_D/I_G, with NH_3-ACF-O10 demonstrating the highest n_D value, reaching 4.33×10^{11} cm^{-2}. In other words, the defect density was significantly increased after plasma modification, which was consistent with the XPS results. Notably, the NH_3-ACF-O10 catalyst exhibited the highest defect density among the catalysts. The XRD spectrum was shown in Fig. S4 (Supporting information). All samples exhibited a typical microcrystalline graphite-like feature with a prominent (002) diffraction peak around 24° and a weaker (100) peak near 43° [44,45], indicating a typical microcrystalline graphite-like structure.

Moreover, the interlayer spacing (d_{002}), and the L_a and L_c values (shown in Figs. 2c-e) increased and decreased for the plasma-modified ACFs, respectively. The decrease in interlayer spacing indicated a reduction in van der Waals forces, potentially enhancing the interaction of reactive species with graphite microcrystals. L_a and L_c were known to represent the average size of graphite crystals in the plane along the a axis, as well as the thickness of graphite planes stacked along the c axis, which was perpendicular to the aforementioned plane. This further confirmed the damage to the surface crystal structure of ACFs caused by plasma modification, suggesting the formation of defects. As depicted in Fig. 2f, the TEM results reveal the previously mentioned increase in layer spacing, while the locally magnified images illustrated the short-range ordering of surface microcrystals and the fracturing of lattice planes, further confirming the formation of defects. Fig. 2g summarized the mechanism of plasma modification and the resulting transformation of the microcrystalline structure of ACFs.

C K-edge NEXAFS spectroscopy was used to gain a more precise understanding of the carbon defects. As depicted in Fig. 3a, the minor peak observed at 288.8 eV was associated to $1s\rightarrow\pi^*$ resonances from oxygen-containing impurities [46]. This indicated an increase in oxygen content in the ACFs after plasma modification, which was in agreement with the XPS results. The spectra (Figs. 3b and c) shown two prominent peaks at 285.5 eV and 291.9 eV, which were attributed to $1s\rightarrow\pi^*$ (C=C bond-ring) transitions and $1s\rightarrow\sigma^*$ (C–C bond-ring) transitions in the sp^2 hybridized network, respec-

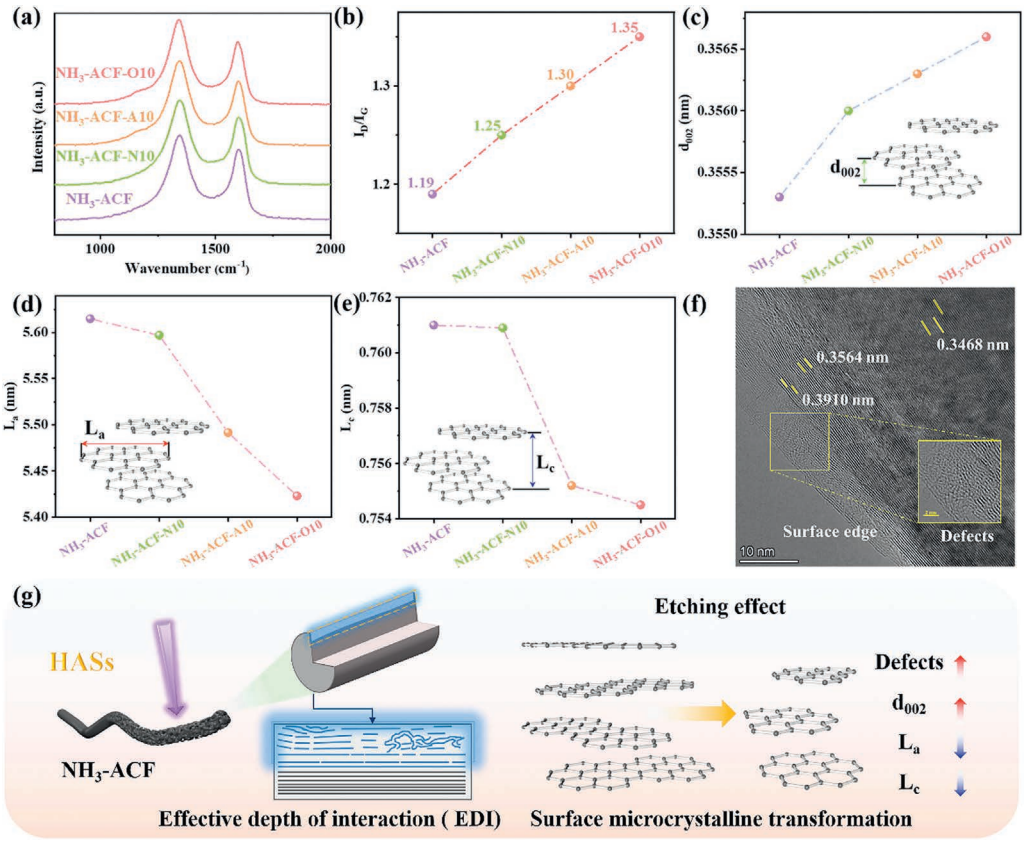


Fig. 2. Raman spectra (a), I_D/I_G values (b), d_{002}, L_a and L_c values (c-e) of ACFs. HRTEM images of NH_3-ACF-O10 (f), and mechanism of plasma modification on microscopic crystal structure (g).

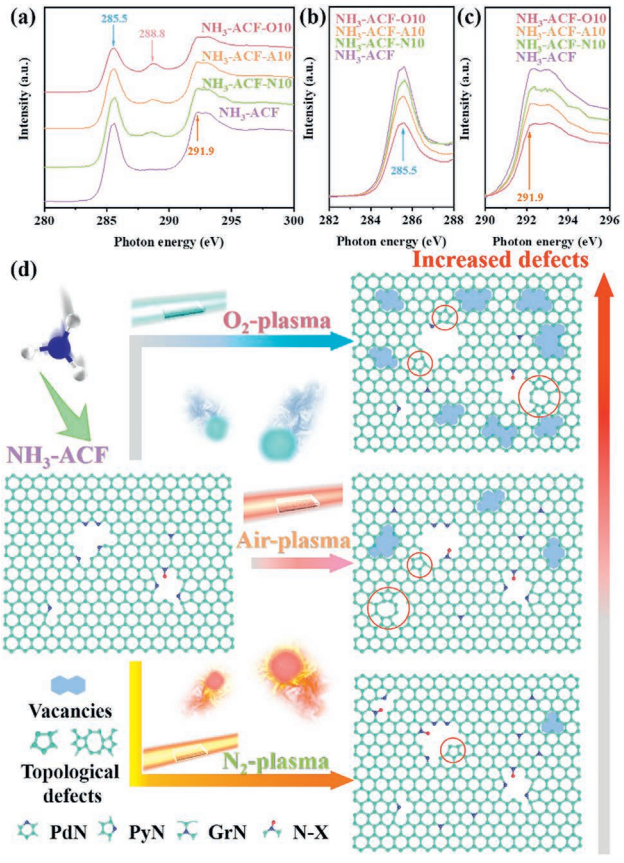


Fig. 3. C K-edge NEXAFS spectra (a), expanded peaks at 285.5 eV (b) and 291.9 eV (c) of ACFs, and schematic diagram of nitrogen species and defects in ACFs (d).

tively [39,47]. These peaks were recognized to be sensitive to strain and distortions in the carbon bonds within the sp^2 hybridized network [48]. Notably, the strength of two dominant peaks decreased significantly after plasma modification, indicating that the carbon matrix was partially disrupted, leading to the formation of surface defects. Additionally, the O_2 plasma modified sample exhibited the weakest peaks, suggesting it possessed the highest number of defects, which aligned with the Raman findings. As previously discussed, the presence of oxygen in the plasma process has been shown to induce partial removal of nitrogen species. Indeed, the removal of doped nitrogen has been demonstrated to create vacancies and induce the formation of topological defects. However, it also indicated that the defects primarily manifested as vacancies, given that the formation of new topological defects would result in a notable enhancement of the π^* feature in the sp^2 hybridized network [39,49], which contrasted with the NEXAFS results. Moreover, Fig. 3d provided a summary of the defects and specific nitrogen heteroatom transitions that occurred following plasma modification. The formed defects caused deviations in graphitic lattice, and the resulting delocalization of π electrons could, in turn, influenced the defects and altered their chemical properties.

Fig. 4a illustrated the catalytic performance of the prepared ACFs. As shown in Fig. 4b, NH_3-ACF achieved the highest sulfur capacity of 0.36 g/g. However, this capacity decreased to 0.27, 0.23, and 0.21 g/g for NH_3-ACF-N10, NH_3-ACF-A10, and NH_3-ACF-O10, respectively. Notably, the pristine ACF (without nitrogen doping) exhibited an exceptionally low sulfur capacity, with a breakout time of less than 10 min, underscoring the crucial role of nitrogen doping in the reaction. In comparison with other studies on nitrogen doping, our sulfur capacity was comparatively minimal, with conventional levels ranging from 0.4 g/g to 1.8 g/g [21,22,24]. This

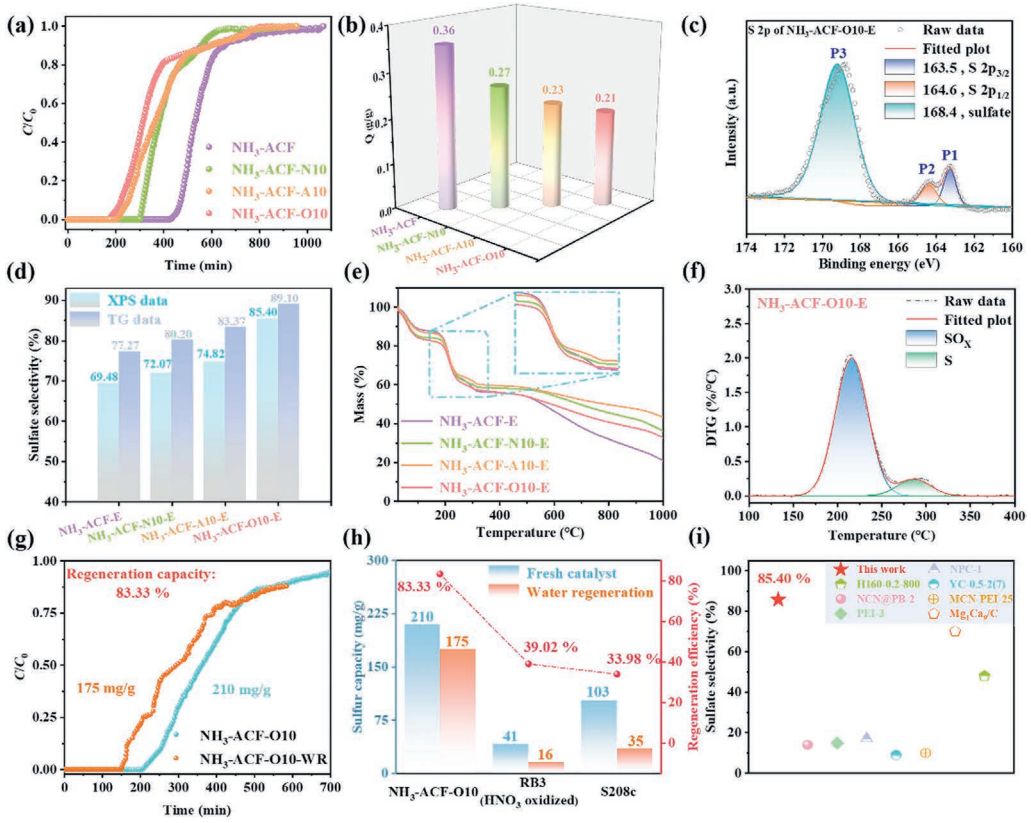


Fig. 4. (a) Breakthrough curves of H_2S on ACFs. (b) H_2S removal capacities of ACFs. (c) S 2p spectrum of NH_3-ACF-O10-E. (d) Sulfate selectivity and SO_x content of ACFs. (e) TG curves of exhausted ACFs. (f) DTG-peak-deafferenting analysis of NH_3-ACF-O10-E. (g) H_2S breakthrough curves over NH_3-ACF-O10 and NH_3-ACF-O10-WR. Comparison of water regeneration (h), and comparison of sulfate selectivity (i).

may be attributed to the comparatively low nitrogen content in our doping.

XPS method was employed to investigate the sulfur-containing products of the reaction. As shown in Fig. 4c and Fig. S5 (Supporting information), the S 2p XPS spectra of all deactivated ACFs were deconvoluted into peaks attributed to elemental sulfur (163.5 and 164.6 eV) and sulfate (168.4 eV) [50], respectively. Notably, the sulfate selectivity varied among the different samples, and the results were presented in Fig. 4d. It was noted that NH_3-ACF exhibited the lowest sulfate selectivity, but it still achieved a notable 69.48 %. Remarkably, the sulfate selectivity increased significantly after plasma modification, reaching 72.07 %, 74.82 % and 85.40 % for NH_3-ACF-N10, NH_3-ACF-A10 and NH_3-ACF-O10, respectively. Additionally, the spent ACFs were analyzed by TG in a N_2 atmosphere. The TG curves (Fig. 4e) shown a distinct weight loss between 150 and 350 °C, signaling the desorption of sulfur species. The derivative thermogravimetric (DTG) curves (Fig. 4f and Fig. S6 in Supporting information) enabled the division of the weight loss into two separate peaks: One at a lower temperature associated with sulfate decomposition, and another at a higher temperature linked to the desorption of elemental sulfur [8,29,51]. It was evident that the weight loss from sulfur oxides was notably higher than that of elemental sulfur across all samples, as shown in Table S2 (Supporting information). Fig. 4d also shown the SO_x content (sulfate selectivity) of all samples which are calculated by peak integration, which was 77.27 %, 80.20 %, 83.37 % and 89.10 % for NH_3-ACF, NH_3-ACF-N10, NH_3-ACF-A10 and NH_3-ACF-O10, respectively. These results were in perfect agreement with the XPS results.

Furthermore, the regeneration performance of NH_3-ACF-O10 was explored using the water wash method, as described in the experimental section in Supporting information. As shown in Fig. 4g, it was noteworthy that 83.33 % of sulfur capacity (175 mg/g) was recovered, indicating that nearly all the generated SO_x were removed from the catalyst surface. The results were also compared with similar studies in literature (Figs. 4h and i). To the best of our knowledge, the present work demonstrated the highest sulfate selectivity [21,22,24,26,29,50], as well as the highest sulfur capacity and regeneration performance based on the water washing regeneration method [52], achieved on carbon materials to date. Although the sulfur capacity progressively declines with regeneration cycles, and achieving near-perfect sulfate selectivity (ideally 100 %) remains a key challenge for practical applications, the high sulfate selectivity, combined with an appropriate sulfur capacity of 0.21 g/g, makes NH_3-ACF-O10 one of the most promising candidates for practical use due to its easy regeneration. In comparison with representative heterogeneous catalysts with alternative regeneration methods, including thermal regeneration, the water-wash method maintains high capacity and regeneration performance (Table S3 in Supporting information). However, several key issues remain to be addressed, such as the primary factors governing sulfur capacity and high sulfate selectivity, as well as the underlying reaction mechanism.

For the reaction, it was assumed that H_2S was initially adsorbed on the basic sites of the catalyst surface, then dissolved into the water layer to form HS^-, which later reacted with reactive oxygen species to produce sulfur-containing compounds [29,53]. As mentioned in the introduction, the porosity, S_{BET}, and surface chemistry could affect the catalytic performance greatly.

As illustrated in Figs. 5a-d, SEM-EDS analysis demonstrated that no large sulfur deposits were observed on the surface of the ACFs, and sulfur-containing species were evenly dispersed throughout the pores. At the same time, ACFs demonstrated structural stabil-

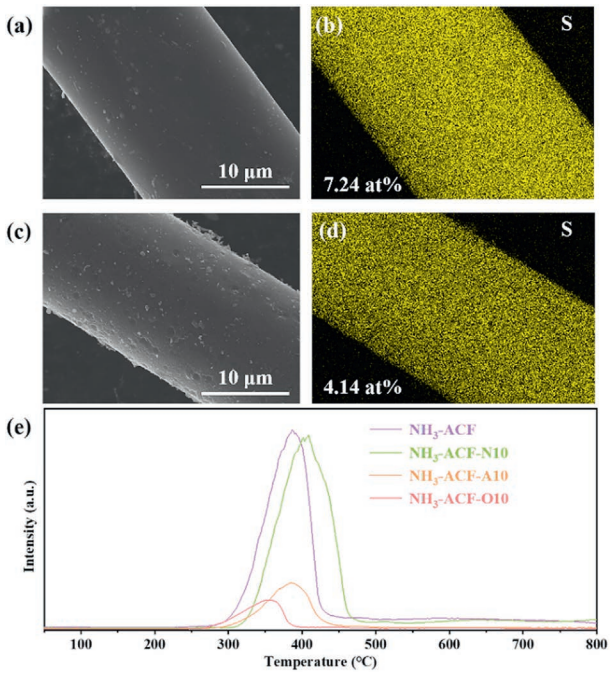


Fig. 5. Elemental mapping images with EDS of NH_3-ACF-E and NH_3-ACF-O10-E (a-d) and H_2S-TPD profiles of ACFs (e).

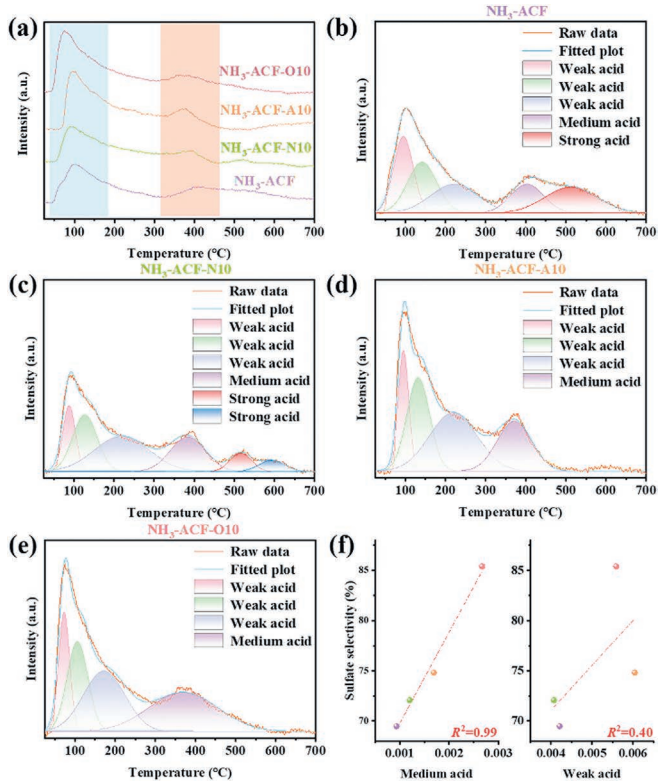


Fig. 6. (a) NH_3-TPD profiles of ACFs. (b-e) TPD-peak-fitting analysis of ACFs, and the relationships between sulfate selectivity and acid of ACFs (f).

ity by maintaining good surface structure even after deactivation. Subsequently, regression analysis was performed to evaluate how pore structure influenced both sulfur capacity and sulfate selectivity. Figs. S7a-d (Supporting information) shown linear fit plots between the sulfur capacity and the V_{tot}, S_{BET}, V_{mic} and V_{mes} of the prepared ACFs, with R^2 values of 0.78, 0.71, 0.77 and 0.68, respectively. Meanwhile, the linear fit plots the sulfate/elemental sulfur content *versus* micropores/mesopores density were displayed in Figs. S7e and f (Supporting information), with R^2 values of 0.20. The statistically insignificant correlation between sulfur capacity/sulfate selectivity and pore structure strongly indicated that the traditionally considered factors, such as V_{tot}, S_{BET}, and V_{mic}, were no longer the primary factors governing sulfur capacity and sulfate formation for the prepared ACFs, respectively [29,30].

The results obtained above provide a rational basis for the assumption that the deposition of sulfur-containing products on the surface basic sites is one primary cause catalyst deactivation before the occurrence of complete pore blockage by sulfur species. In essence, the surface basicity, as opposed to conventional parameters of pore structure, emerges as the pivotal factor determining sulfur capacity. It was strongly supported by the positive and negative correlation between PdN content and sulfur capacity and sulfate selectivity, respectively (Fig. S8 in Supporting information). Furthermore, the H_2S-TPD (Fig. 5e) indicated that H_2S was chemisorbed on the catalyst surface. The gradual weakening of the desorption peak supports the hypothesis that surface basicity decreased after plasma modification, which is consistent with the observed decrease in both sulfur capacity and PdN content.

Meanwhile, surface acidity may also influence sulfate selectivity, similar to the previously mentioned limitation of basic sites. To investigate the effect of surface acidity and acid type on sulfate selectivity, NH_3-TPD and Py-IR analyses were performed. As shown in Fig. 6a, the NH_3 desorption profile was categorized into three regions: weak acid sites below 300 °C, medium acid sites between 300 °C and 500 °C, and strong acid sites above 500 °C [54,55]. Figs. 6b-e display the fitted curves for peak splitting, and the corresponding NH_3 desorption peak areas were quantified and compiled in Table S4 (Supporting information). It was evident that both weak acidity and medium acidity were significantly enhanced in plasma-modified samples, primarily due to the transformation of oxygen-containing functional groups. NH_3-ACF-A10 and NH_3-ACF-O10 exhibited the highest amounts of weak and medium acid sites, respectively, along with the disappearance of strong acid sites. This is because oxygen-containing, high-energy active substances generated by Air and O_2 plasma can oxidize the strong acidic sites, which typically contain unstable, oxygen-containing functional groups. These high-energy active substances then react with free radicals or unsaturated bonds on the carbon surface, forming new weak and medium acid sites [56]. In contrast, N_2 plasma tends to dope nitrogen atoms into the carbon matrix, achieving surface acid-base regulation without directly affecting the strong acid sites [57]. It has been demonstrated that when pH < 4.5, physical adsorption of H_2S does not dissolve in the water film. In the range of 4.5 < pH < 7, the dissociation of H_2S is inhibited, promoting sulfate formation [8]. In the present work, the correlation between the acid sites on the catalyst surface and sulfate selectivity is clear. Regression analysis (Fig. 6f) shows that medium acid sites significantly influence sulfate selectivity ($R^2 = 0.99$), while the influence of weak acid sites is negligible ($R^2 = 0.40$). As anticipated, medium acid sites exhibit a negative correlation with sulfur capacity, reflecting the inherent trade-off between sulfur capacity and sulfate selectivity.

The Py-IR spectra were shown in Fig. 7a. As observed, six bands were detected in the 1300–1700 cm^{-1} region, absorption peaks were identified for Lewis acid sites at 1450, 1609, and 1620 cm^{-1}, for Brønsted acid sites at 1540 and 1640 cm^{-1}, and a combined band at 1490 cm^{-1}, which corresponded to pyridine adsorption on both Lewis and Brønsted acid sites [58–60]. It was evident that Lewis acid sites were the predominant acidic sites in all synthesized samples, with their concentration notably increased follow-

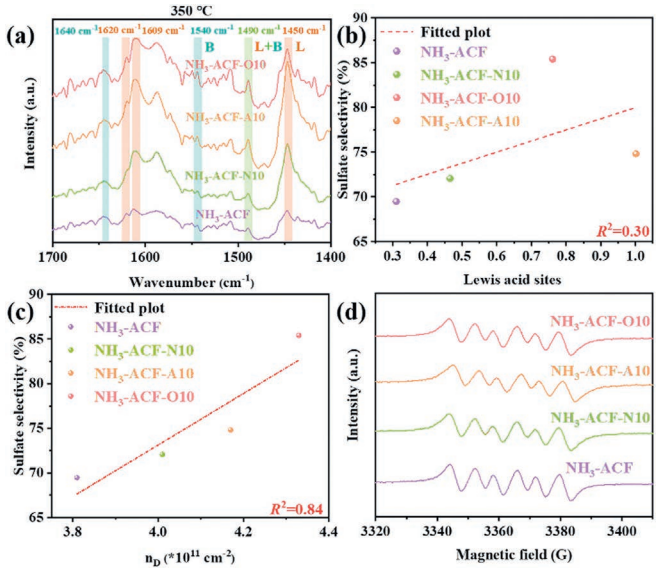


Fig. 7. (a) Pyridine-IR spectra of ACFs at 350 °C. (b) Relationships between sulfate selectivity and Lewis acid sites of ACFs. Relationships between sulfate selectivity and the value of n_D (c), and EPR spectra of ACFs (d).

ing plasma treatment. However, contrary to expectations, NH_3-ACF-A10, rather than NH_3-ACF-O10, exhibited the highest Lewis acid sites concentration, which contradicts with the trends observed for sulfur capacity and sulfate selectivity. This observation suggested that the strength of the acid sites, *i.e.*, medium acid rather than their type, was a key factor influencing catalytic performance. The poor linear correlation (R^2=0.30) between sulfate selectivity and the content of Lewis acid sites (Fig. 7b) further supported this conclusion.

The influence of defects on sulfate selectivity was also investigated. As illustrated in Fig. 7c, a significant linear correlation between the n_D ratio and sulfate selectivity was observed, with an R^2 value of 0.84. This indicated that defects undeniably had a considerable impact on sulfate formation. And the influence perhaps due mainly to the catalytically generating oxygen-containing free radicals with strong oxidative capabilities, which could directly oxidize H_2S to sulfate. As demonstrated in Fig. S9 (Supporting information), the EPR signal intensity of the reaction oxygen vacancy (g = 2.003) content in the catalyst gradually increases with the increase in defect density. The appearance of $O_2^{\bullet-}$ signals in the EPR spectra of all the samples (Fig. 7d) further confirms the formation of superoxide radicals during the reaction process. Specifically, the electrons accumulated at the carbon atoms exposed around vacancies, which then reduced the adsorbed O_2 to $O_2^{\bullet-}$ [61]. Furthermore, doped nitrogen atoms (PdN and PyN) in the carbon matrix, due to the localized unpaired electrons, could activate O_2 to form oxygen-containing free radicals. This activation occurred through the conjugation and enhanced migration of π^* electrons in the adjacent sp^2 carbon [24,34,62].

Thus, it was clear that the further reduction of basic sites was responsible for the relative low sulfur capacity, while the enhanced surface acidity, especially medium acid, together with the increased defect density were contributed to the high sulfate selectivity.

As is well known, oxygen was crucial for the reaction, however it must first be activated into reactive oxygen species because of the stability of its triplet state with spin-paired electrons [9]. It was believed that chemically adsorbed oxygen species, oxygen-containing group, and oxygen radicals could be served as reactive oxygen species. Furthermore, it has been shown that $O_2^{\bullet-}$ could in-

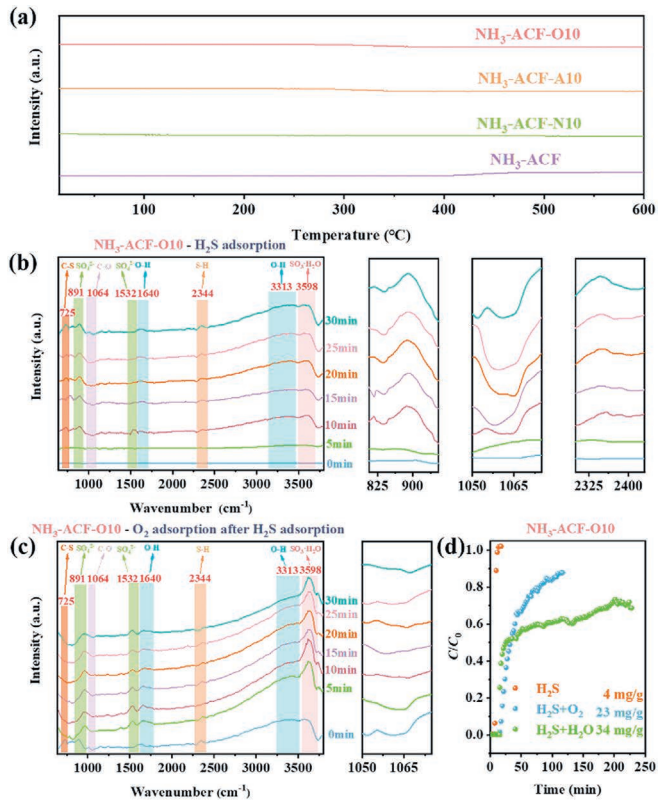


Fig. 8. (a) O_2-TPD-MS profiles of ACFs. *In situ* DRIFTS spectra for H_2S adsorption (b) and O_2 adsorption after H_2S adsorption on NH_3-ACF-O10 (c), and breakthrough curves over NH_3-ACF-O10 under different conditions (d).

deed be generated by defects and enhance the formation of sulfate. However, it remains necessary to investigate whether the other reactive oxygen species also participate during the reaction.

As depicted in Fig. 8a, no O_2 desorption peak was detected in the O_2-TPD spectra of any of the samples, indicating that the ACFs surface could not form chemically adsorbed oxygen. In other words, molecular oxygen was adsorbed exclusively at defect and further activated by defect to form $O_2^{\bullet-}$. Indeed, it has proved that oxygen-containing functional groups could participate in the reaction and exert a dominant influence. Therefore, *in situ* DRIFTS was carried out to investigate the role of oxygen containing group. As shown in Fig. 8b, when only H_2S was present in the atmosphere, the gradually intensified peak at 2344 cm^{-1}, corresponding to the stretching of the H-S bond in H_2S [14], were detected, indicating the adsorption of H_2S on the surface. Additionally, the appearance of peaks at 1640 and 3313 cm^{-1}, which corresponded to O–H stretching in H_2O, together with the depletion peak at 1064 cm^{-1} related to the C–O species, strongly suggested that the adsorbed H_2S reacted with the C–O group on the surface to form water and sulfur-containing species. This suggested that the oxygen-containing function group were involved in the reaction. Furthermore, the peaks at 3598, 1532 and 891 cm^{-1} were mainly ascribed to the formation of sulfur oxides, specifically $SO_3{\cdot}H_2O$, S=O for tridentate sulfate, and O-S-O for chelating bidentate sulfate, respectively [21,63,64]. These findings were in perfect agreement with the above-mentioned assumption. Fig. 8c shown the infrared spectrum after introducing O_2 into the atmosphere following H_2S adsorption. It was clearly observed that the consumed C–O was recovered, indicating that oxygen-containing functional groups can be regenerated by molecule O_2.

Concurrently, the extent of the participation of oxygen-containing functional groups in the reaction was investigated. The

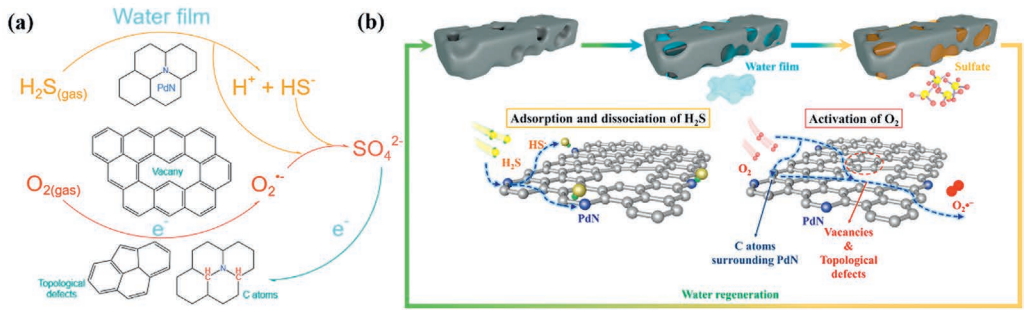


Fig. 9. Schematic illustration of the catalytic oxidation of H_2S at room temperature on NH_3-ACF-O10.

related breakthrough curves were presented in Fig. 8d. It was evident that sulfur capacity of the catalyst was rather low when O_2 was absent, amounting to 34 mg/g comparing to 210 mg/g when O_2 was involved in the reaction. This was also in sharp contrast to the literature result, where the catalyst exhibited a sulfur capacity in the presence of H_2S and H_2O that was comparable to that in a coexisting system of H_2S, H_2O, and O_2 when the oxygen containing group was regarded as the main reactive oxygen species. Thus, the possibility of oxygen containing group was the main reactive oxygen species could also be excluded. Furthermore, when only H_2S and O_2 were introduced into the reaction simultaneously, even with a modest amount of functional group regeneration facilitated by oxygen, there was a negligible contribution to the sulfur capacity (23 mg/g). This led to the conclusion that the $O_2^{\bullet-}$ was thought the main reactive oxygen species for the reaction. And water played an important role in the reaction, which not only formed water film that dissolved adsorbed H_2S and reactive oxygen species, but also acted as a conveyor belt to transport the generated sulfur species for storage on the surface and within the pore channels.

Based on the above analysis, the reaction mechanism over the prepared ACFs could be tentatively proposed as following (Fig. 9):

(1) H_2S was chemisorbed on the basic sites of catalysts, *i.e.*, the doped N species, specially PdN species. However, the adsorption capacity was relatively low due to the low content of PdN content. Finally, the adsorbed H_2S dissolved in the water film in the form of HS^-.
(2) the molecular O_2 was adsorbed on the defects (mainly in the form of vacancy), where the adsorbed oxygen acquired electrons and reduced to $O_2^{\bullet-}$. Subsequently, the formed $O_2^{\bullet-}$ dissolved in the water film.
(3) the dissolved HS^- reacted with the $O_2^{\bullet-}$ with strong oxidative capabilities to formed sulfate via isolated sulfur radical intermediate product. Meanwhile, a little fraction of isolated sulfur radicals collided with each other to form elemental S_8. Additionally, the collision probability of isolated sulfur radical was greatly limited due to the poor H_2S adsorption capacity, namely low isolated sulfur radical generation, and enhanced surface acidity of the catalyst. Therefore, the generation of elemental sulfur was restricted, which in turn facilitated the further reaction of isolated sulfur radical to form sulfate.

Therefore, the reaction process obeyed a Langmuir-Hinshelwood (L-H) like mechanism. As is known, the L-H mechanism usually means that the reaction occurred via two chemisorbed molecules [65]. However, for this reaction, it was proceeded *via* chemisorbed H_2S and superoxide radical, which was adsorbed and activated by defect.

In summary, ACFs with high sulfate selectivity and optimal sulfur capacity were prepared through a synergistic strategy of "nitrogen doping - defect engineering". Among the prepared catalyst, NH_3-ACF-O10 presented the best catalytic performance, which could achieve sulfur capacity of 0.21 g/g, sulfate selectivity of 85.40 %, and outstanding water wash regeneration performance, *i.e.*, 83.33 % sulfur capacity could be recovered. The sulfur capacity was mainly depended on the content of N species, especially PdN species. The low content of PdN species for the prepared ACFs meant that limited amount of H_2S could be adsorbed and participate in the reaction, leading to the relatively low sulfur capacity. Meanwhile, the enhanced surface acidity, especially medium acid, together with the increased defect density after plasma modification were responsible for the high sulfate selectivity. The enhanced surface acidity could greatly decrease the collision probability of isolated sulfur radical, subsequently, restricting the formation of elemental sulfur and benefiting the formation of sulfate, which was in turn further decrease the sulfur capacity. Simultaneously, the molecular O_2 was adsorbed exclusively at defects and further activated by defects to form $O_2^{\bullet-}$ with strong oxidative capabilities, which could oxidize adsorbed H_2S to sulfate directly. Moreover, based on the previous work, it was thought that the defects, *i.e.*, the formation of $O_2^{\bullet-}$, played a curial role in the formation of sulfate. Besides, it was thought that $O_2^{\bullet-}$ were the main reactive oxygen species for the reaction. Moreover, the reaction obeyed a L-H like mechanism, the reaction was proceeded via chemisorbed H_2S and $O_2^{\bullet-}$. However, although relative high sulfate selectivity was obtained for the prepared catalysts, it is critical to note that achieving near-perfect sulfate selectivity (ideally 100 %) remained a key challenge for practical applications.

Declaration of competing interest

The authors declare that they have no known competing financial interests or personal relationships that could have appeared to influence the work reported in this paper.

CRediT authorship contribution statement

Yue Liu: Writing – original draft, Visualization, Investigation, Formal analysis. **Linhong Wen:** Investigation, Data curation. **Mengyan Wang:** Validation, Investigation. **Jianxiao Yang:** Writing – review & editing, Resources, Project administration, Funding acquisition. **Xin Zhang:** Writing – review & editing, Resources, Project administration, Methodology, Funding acquisition, Conceptualization.

Acknowledgments

This work was supported by the National Natural Science Foundation of China (Nos. 22276191, 52372044 and 21976177), National Key Research and Development Program of China (No. 2022YFB4101500), Shccig-Qinling Program Found (No.

SMYJY20230072), Postgraduate Scientific Research Innovation Project of Hunan Province (No. LXBZZ2024044) and CNPC Innovation Found (No. 2022DQ02–0411).

Supplementary materials

Supplementary material associated with this article can be found, in the online version, at doi:10.1016/j.cclet.2025.112153.

References

[1] B. Tansel, B. Inanloo, Waste Manage. 88 (2019) 39–47.
[2] E. Nie, G. Zheng, D. Gao, et al., Sci. Total Environ. 659 (2019) 664–672.
[3] P. Jin, Y. Gu, X. Shi, W. Yang, Biotechnol. Biofuels 12 (2019) 100.
[4] M. Yin, S.C. Pillai, N. Bolan, et al., Chem. Eng. J. 479 (2024) 147854.
[5] I. Omri, H. Bouallagui, F. Aouidi, J.J. Godon, M. Hamdi, Bioresour. Technol. 102 (2011) 10202–10209.
[6] C. Yang, Y. Wang, H. Fan, et al., Appl. Catal. B 266 (2020) 118674.
[7] J. Wang, L. Wang, H. Fan, et al., Fuel 209 (2017) 329–338.
[8] T.J. Bandosz, J. Colloid Interface Sci. 246 (2002) 1–20.
[9] Y. Chao, W. Yeshuang, L. Meisheng, et al., Appl. Catal. B 323 (2023) 122133.
[10] X. Zheng, Y. Li, Y. Zheng, et al., ACS Catal. 10 (2020) 3968–3983.
[11] X. Zheng, B. Li, L. Shen, et al., Appl. Catal., B 329 (2023) 122526.
[12] X. Zheng, G. Lei, S. Wang, et al., ACS Catal. 13 (2023) 11723–11752.
[13] J.R. Kastner, K.C. Das, Q. Buquoi, N.D. Melear, Environ. Sci. Technol. 37 (2003) 2568–2574.
[14] A. Ros, M.A. Montes-Moran, E. Fuente, D.M. Nevskaia, M.J. Martin, Environ. Sci. Technol. 40 (2006) 302–309.
[15] S.P. Hernández, M. Chiappero, N. Russo, D. Fino, Chem. Eng. J. 176-177 (2011) 272–279.
[16] G. Lei, D. Li, Y. Ma, et al., Carbon 210 (2023) 118039.
[17] G. Lei, Z. Fan, Y. Hou, et al., J. Environ. Chem. Eng. 11 (2023) 109095.
[18] G. Lei, S. Qi, H. Li, et al., Phys. Chem. Chem. Phys. 25 (2023) 32317–32322.
[19] G. Lei, X. Lin, H. Yan, et al., ACS Catal. 14 (2024) 17103–17112.
[20] F. Sun, J. Liu, H. Chen, et al., ACS Catal. 3 (2013) 862–870.
[21] L. Chen, X. Jiang, S. Ma, et al., Chem. Eng. J. 475 (2023) 146115.
[22] L. Chen, J. Yuan, T. Li, et al., Sci. Total Environ. 768 (2021) 144452.
[23] S. Cheng, T. Wang, L. Chu, J. Li, L. Zhang, Sci. Total Environ. 915 (2024) 170073.
[24] J. Wu, W. Chen, L. Chen, X. Jiang, J. Hazard. Mater. 424 (2022) 127648.
[25] M.S. Shah, M. Tsapatsis, J.I. Siepmann, Chem. Rev. 117 (2017) 9755–9803.
[26] K. Li, X. Chen, X. Qin, et al., Sep. Purif. Technol. 332 (2024) 125790.
[27] Z. Wang, J. Huang, Y. Zhong, et al., Fuel 319 (2022) 123774.
[28] A. Bagreev, T.J. Bandosz, Carbon 39 (2001) 2303–2311.
[29] Q. Chen, Z. Wang, D. Long, et al., Ind. Eng. Chem. Res. 49 (2010) 3152–3159.
[30] Y. Liu, M. Wang, J. Yang, et al., Fuel 368 (2024) 131590.
[31] Y. Pan, H. Xu, M. Chen, et al., ACS Catal. 11 (2021) 5974–5983.
[32] Y. Jiao, Y. Zheng, M. Jaroniec, S.Z. Qiao, J. Am. Chem. Soc. 136 (2014) 4394–4403.
[33] Y. Zhao, J. Wan, H. Yao, et al., Nat. Chem. 10 (2018) 924–931.
[34] G. Qu, P. Jia, T. Zhang, et al., Chem. Eng. J. 475 (2023) 145888.
[35] W. Wei, F. Wang, J. Yang, et al., ACS Appl. Mater. Interfaces 13 (2021) 6557–6565.
[36] K.S.W. Sing, Pure Appl. Chem. 57 (1985) 603–619.
[37] T. Zhang, S. Zuo, Environ. Sci. Pollut. Res. 30 (2023) 45097–45111.
[38] Y. Huang, Q. Yu, M. Li, et al., Chem. Eng. J. 418 (2021) 129474.
[39] Y. Dong, Q. Zhang, Z. Tian, et al., Adv. Mater. 32 (2020) 2001300.
[40] J. Zhu, S. Mu, Adv. Funct. Mater. 30 (2020) 2001097.
[41] A. Cabrera-Codony, M.A. Montes-Morán, M. Sánchez-Polo, M.J. Martín, R. Gonzalez-Olmos, Environ. Sci. Technol. 48 (2014) 7187–7195.
[42] J.R. Pels, F. Kapteijn, J.A. Moulijn, Q. Zhu, K.M. Thomas, Carbon 33 (1995) 1641–1653.
[43] L.G. Cançado, A. Jorio, E.H.M. Ferreira, et al., Nano Lett. 11 (2011) 3190–3196.
[44] M.A. Short, P.L. Walker, Carbon 1 (1963) 3–9.
[45] F. Sun, X. Liu, H.B. Wu, et al., Nano Lett. 18 (2018) 3368–3376.
[46] F.L. Coffman, R. Cao, P.A. Pianetta, S. Kapoor, M. Kelly, L.J. Terminello, Appl. Phys. Lett. 69 (1996) 568–570.
[47] Y. Zheng, Y. Jiao, Y. Zhu, et al., Nat. Commun. 5 (2014) 3783.
[48] A. Milev, N. Tran, K. Kannangara, M. Wilson, Sci. Technol. Adv. Mater. 7 (2006) 834–838.
[49] C. Wang, D. Liu, S. Chen, et al., Small 12 (2016) 5684–5691.
[50] J. Wang, C. Ke, X. Jia, et al., Appl. Catal. B 283 (2020) 119650.
[51] R. Yan, T. Chin, Y.L. Ng, et al., Environ. Sci. Technol. 38 (2004) 316–323.
[52] F. Adib, A. Bagreev, T.J. Bandosz, Ind. Eng. Chem. Res. 39 (2000) 2439–2446.
[53] J. Klein, K.-D. Henning, Fuel 63 (1984) 1064–1067.
[54] Z. Wang, K. Xie, B. Jiang, S. Zuo, Q. Wang, J. Hazard. Mater. 435 (2022) 128950.
[55] X. Zhang, K. Yue, R. Rao, et al., Appl. Catal. B 310 (2022) 121300.
[56] J.P. Boudou, A. Martinez-Alonzo, J.M.D. Tascon, Carbon 38 (2000) 1021–1029.
[57] G. Su, Y. He, L. Xie, et al., Ind. Crops Prod. 215 (2024) 118607.
[58] J. An, Y. Wang, J. Lu, et al., J. Am. Chem. Soc. 140 (2018) 4172–4181.
[59] V. Boosa, S. Varimalla, M. Dumpalapally, et al., Appl. Catal. B 292 (2021) 120177.
[60] S. Lijuan, Z. Xiaohai, L. Ganchang, et al., Chem. Eng. J. 346 (2018) 238–248.
[61] Z. Liu, Z. Zhao, Y. Wang, et al., Adv. Mater. 29 (2017) 1606207.
[62] V.V. Strelko, V.S. Kuts, P.A. Thrower, Carbon 38 (2000) 1499–1503.
[63] A. Givan, A. Loewenschuss, C.J. Nielsen, M. Rozenberg, J. Mol. Struct. 830 (2007) 21–34.
[64] M. Waqif, P. Bazin, O. Saur, et al., Appl. Catal. B 11 (1997) 193–205.
[65] D. Kiani, I.E. Wachs, ACS Catal 14 (2024) 16551–17208.